UNIVERSITY OF LEEDS

This is a repository copy of *Kinetics of O3 with Ca+ and Its Higher Oxides CaOn+ (n = 1–3) and Updates to a Model of Meteoric Calcium in the Mesosphere and Lower Thermosphere*.

White Rose Research Online URL for this paper:
https://eprints.whiterose.ac.uk/198808/

Version: Accepted Version

Article:

Shuman, NS, Sweeny, BC, Viggiano, AA et al. (5 more authors) (2023) Kinetics of O3 with Ca+ and Its Higher Oxides CaOn+ (n = 1–3) and Updates to a Model of Meteoric Calcium in the Mesosphere and Lower Thermosphere. The Journal of Physical Chemistry A, 127 (18). pp. 4043-4054. ISSN 1089-5639

https://doi.org/10.1021/acs.jpca.3c01126

© 2023 American Chemical Society. This is an author produced version of an article published in The Journal of Physical Chemistry A. Uploaded in accordance with the publisher's self-archiving policy.

Reuse

Items deposited in White Rose Research Online are protected by copyright, with all rights reserved unless indicated otherwise. They may be downloaded and/or printed for private study, or other acts as permitted by national copyright laws. The publisher or other rights holders may allow further reproduction and re-use of the full text version. This is indicated by the licence information on the White Rose Research Online record for the item.

Takedown

If you consider content in White Rose Research Online to be in breach of UK law, please notify us by emailing eprints@whiterose.ac.uk including the URL of the record and the reason for the withdrawal request.

White Rose
university consortium
Universities of Leeds, Sheffield & York

eprints@whiterose.ac.uk
https://eprints.whiterose.ac.uk/

Kinetics of O_3 with Ca^+ and its Higher Oxides CaO_n^+ (n = 1-3) and Updates to a Model of Meteoric Calcium in the Mesosphere and Lower Thermosphere

Nicholas S. Shuman[1,*] Brendan C. Sweeny[2], Albert A. Viggiano,[1] John M. C. Plane,[3] Wuhu Feng,[3,4] Anton Lachowicz,[1] Michael C. Heaven,[5] and Shaun G. Ard,[1,*]

[1]*Air Force Research Laboratory, Space Vehicles Directorate, Kirtland Air Force Base, New Mexico 87117, USA*
[2]*Boston College Institute for Scientific Research, Boston, MA 02549, USA*

[3]*School of Chemistry, University of Leeds, United Kingdom.*

[4] *National Centre for Atmospheric Science and School of Earth and Environment, University of Leeds, United Kingdom.*

[5] *Department of Chemistry, Emory University, Atlanta, GA 30322, USA*

* *Corresponding authors: rvborgmailbox@us.af.mil*

Abstract

The room-temperature rate constants and product branching fractions of CaO_n^+ (n = 0 – 3) + O_3 are measured using a selected-ion flow tube (SIFT) apparatus. The Ca^+ + O_3 produces CaO^+ + O_2 with $k = 9 \pm 4 \times 10^{-10}$ cm^3 s^{-1}, within uncertainty equal to the Langevin capture rate constant. This value is significantly larger than several literature values. Most likely those values were underestimated due to reformation of Ca^+ from sequential chemistry of higher calcium oxide cations with O_3, as explored here. A rate constant of $8 \pm 3 \times 10^{-10}$ cm^3 s^{-1} is recommended. Both CaO^+ and CaO_2^+ react near the capture rate constant with ozone. The CaO^+ reaction yields both CaO_2^+ + O_2 (0.80 ±0.15 branching) and Ca^+ + 2 O_2. Similarly, the CaO_2^+ reaction yields both CaO_3^+ + O_2 (0.85 ±0.15 branching) and CaO^+ + 2 O_2. CaO_3^+ + O_3 yields CaO_2^+ + 2 O_2 at $2 \pm 1 \times 10^{-11}$ cm^3 s^{-1}, about 2% of the capture rate constant. The results are supported using density functional calculations and statistical modeling. In general, CaO_n^+ + O_3 yields CaO_{n+1}^+ + O_2, i.e., the expected oxidation. Some fraction of the CaO_{n+1}^+ is produced with sufficient internal energy to further dissociate to CaO_{n-1}^+ + O_2, yielding the same products as the oxidation of O_3 by CaO_n^+. Mesospheric Ca and Ca^+ concentrations are modeled as a function of day, latitude, and altitude using the Whole Atmosphere Community Climate Model (WACCM); incorporating the updated rate constants improves agreement with concentrations derived from lidar measurements.

Introduction

The ablation of meteoroids entering the Earth's atmosphere produces significant concentrations of metals at altitudes below 120 km.[1,2] These metals, primarily Fe, Mg, Si, and Na, with smaller amounts of Ca, and K, form partially ionized layers of atoms and atomic cations that slowly descend. The layers can cause Sporadic E, vertically thin layers of enhanced electron density that affect radio wave propagation.[3] Ca, despite being in lower neutral abundance than other metals, is of particular interest. It has a much larger degree of ionization than the other meteoric metals, and it is the only meteoric metal for which both neutral and ion concentrations can be quantified by ground-based lidar (quantification of other ionic metals have resonance transitions only at smaller wavelengths where the stratosphere is opaque, e.g., Na^+).[4,5] Because the various metal, metal ion, and electron concentrations roughly track each other, calcium lidar measurements are a proxy for the behavior of the more abundant metals. Full models of Ca and Ca^+ chemistry and physics in the mesosphere and lower thermosphere have been developed, most recently using the Whole Atmosphere Community Climate Model (WACCM).[6]

In this region, the primary process converting ionized Ca^+ to neutral Ca is

$$Ca^+ + O_3 \rightarrow CaO^+ + O_2 \tag{1}$$

followed by rapid dissociative recombination

$$CaO^+ + e^- \rightarrow Ca + O. \tag{2}$$

The importance of atomic metal cation reactions with ozone was recognized early in the space age as efforts to decipher the chemistry of the ionosphere progressed. Eldon Ferguson and Fred Fehsenfeld, having developed the flowing afterglow technique to measure ion-molecule reaction kinetics, reported room temperature rate constants for several meteoric metals with ozone. Na^+ and K^+ were observed not to measurably react, which was expected as their respective M^+-O bond energies are smaller than that of O_2-O (102.45 ±0.04 kJ mol^{-1})[7] and the reactions analogous to reaction 1 are endothermic.[8] Fe^+, Mg^+, and Ca^+ were all reported to react with ozone at 10 – 20% of the calculated Langevin-Gioumousis-Stevenson (LGS)[9] capture rate constant. However, the rate constants for both the Fe^+ [10] and Mg^+ [11] reactions were later found to be underestimated, and in fact occur near the capture rate. In both cases, the underestimation was due to an analysis assuming pseudo-first order, single exponential decay of the primary ion without accounting for the surprisingly complex sequential chemistry that occurs in these systems.

In general, a metal oxide cation MO^+ can react with ozone via

$$MO_n^+ + O_3 \rightarrow MO_{n+1}^+ + O_2 \tag{3a}$$

$$\rightarrow MO_{n-1}^+ + 2\ O_2. \tag{3b}$$

Reactions of type 3b can lead to reformation of M^+ and, if not accounted for, an artificially small rate constant for the decay of the primary ion.

Reaction 3a is the oxidation of MO_n^+ by ozone, but reaction 3b is equivalent to an oxidation *of* ozone by MO^+. We have previously discussed this mechanism in the reactions of Fe^+, Ni^+, Sm^+, and Nd^+ with ozone.[10,12,13] We have suggested that reaction 3b can be described by

$$MO_n^+ + O_3 \rightarrow MO_n^+(O_3)^* \tag{4a}$$

$$MO_n^+(O_3)^* \rightarrow MO_{n+1}^{+*} + O_2 \tag{4b}$$

$$MO_{n+1}^{+*} \rightarrow MO_{n-1}^{+} + O_2 . \tag{4c}$$

$$\rightarrow MO_{n+1}^{+} \tag{4d}$$

MO_n^+ and O_3 form a highly internally excited entrance complex (reaction 4a) that undergoes dissociation (reaction 4b), losing O_2 and leaving an oxidized MO_{n+1}^{+*} product. The product energy distribution will sometimes leave the MO_{n+1}^{+*} product with sufficient energy to dissociate a second O_2 (reaction 4c) and a now reduced MO_{n-1}^{+} product. To distinguish this process from a direct reduction of the metal oxide, we will use the term dissociative oxidation. When larger amounts of product energy remain in the O_2 or in translation, MO_{n+1}^{+*} has too little energy to dissociate further and becomes stabilized (reaction 4d) either by radiation or collision.

The $Ca^+ + O_3$ rate constant has been measured several times using different methods. The early flowing afterglow study[8] reported a rate constant of 1.6×10^{-10} cm^3 s^{-1} with uncertainty estimated as a factor of 2. Curvature (i.e., not a single exponential decay) is apparent in the Ca^+ decline and is attributed to a background signal. The same study reported a $Mg^+ + O_3$ rate constant of 2×10^{-10} cm^3 s^{-1}, that the group corrected to 7×10^{-10} cm^3 s^{-1} in a later study[11] that accounted for the $MgO^+ + O_3 \rightarrow Mg^+ + 2\,O_2$ reaction. A selected-ion flow tube (SIFT) study[14] reported values of $4.7 \pm 1.4 \times 10^{-10}$ cm^3 s^{-1} and $4.9 \pm 1.5 \times 10^{-10}$ cm^3 s^{-1} using two different ion sources. An inductively-coupled plasma (ICP) source yielded Ar^+ isobaric with Ca^+ at the resolution of the experiment, complicating the analysis, and the $Ca^+ + O_3$ rate constant was derived only from data at large extent of reaction where there was confidence that the Ar^+ has reacted away. An electrospray ion source did not have this complication, but the data presented shows curvature in the Ca^+ decay, while the published fit to the data is a single exponential that compromises by overestimating the Ca^+ at small extent of reaction and underestimating it at larger extent of reaction. Sequential chemistry was considered in the analysis, with lower limits on rate constants for reactions 5a

$$CaO^+ + O_3 \rightarrow CaO_2^+ + O_2 \tag{5a}$$

$$\rightarrow Ca^+ + 2O_2 \tag{5b}$$

and 6a

$$CaO_2^+ + O_3 \rightarrow CaO_3^+ + O_2 \tag{6a}$$

$$\rightarrow CaO^+ + 2O_2 \tag{6b}$$

near the capture rate. The same work considered the dissociative oxidation reactions like 3b, 5b, and 6b, for other reactants, but apparently determined that these were not occurring in the $Ca^+ + O_3$ system. Finally, a study monitoring the Ca^+ decay using laser-induced fluorescence (LIF) reported a temperature-independent (189 – 312 K) rate constant for reaction 1 of $3.9 \pm 1.2 \times 10^{-10}$ cm^3 s^{-1}.[15] Again, the dissociative oxidation reaction 5b was considered in the analysis but determined not to be significantly occurring as the Ca^+ signal decay was best fit by a single exponential. The sub-collisional rate constant was rationalized by a symmetry restriction preventing dissociation of the entrance complex when formed by co-planar approach.

Despite the good agreement between the various measurements, underestimation of $M^+ + O_3$ rate constants has been endemic in the literature.[10,11] Here, we reinvestigate the $Ca^+ + O_3$ system using a SIFT apparatus. We aim both to evaluate the rate constant of reaction 1 and to determine the mechanism(s) of reactions 5 and 6. To this end, the experimental results are supported by density functional calculations of the various reaction coordinates and by statistical modeling. The atmospheric implications are determined by incorporating the updated rate constants into the previously developed WACCM model.

Methods

Selected-ion flow tube

The experiments were carried out using the variable-ion source, temperature-adjustable selected-ion flow tube (VISTA-SIFT) apparatus that has been described in detail elsewhere.[16] Ca^+ ions were produced in a ESI source. A 10 mM solution of $CaCl_2$ (Sigma Aldrich) was prepared in methanol. The solution was sprayed in atmosphere through a 50 µm fused silica capillary held at 4 kV. Ions were accelerated into vacuum through a 4 mm aperture to the entrance of an ion funnel. The extent of the ions was compressed using the funnel and transported using a rectilinear (i.e., rods of square cross-section) quadrupole ion guide and a quadrupole ion bender. The 40 Da ions were mass-selected using a quadrupole mass filter and transported further using a series of trapezoidal (i.e., decreasing inscribed diameter along the length) rectilinear quadrupole ion guides. The final ion guide was coupled to a Venturi inlet and the ions were injected into a stainless-steel flow tube operated at 0.35 Torr. Pressure was maintained by a 10 std. L min^{-1} metered helium flow (MKS Instruments) entering through a "showerhead" of 0.5 mm diameter holes surrounding the exit of the final ion guide. The final two ion guides, which operated at pressures above 1 mTorr, were operated with "asymmetric rods", i.e., rods interleaved between the quadrupole rods angled to have a decreasing inscribed diameter along the length. A DC voltage on these rods provided a gradient to the center line potential of the ion guides to transport the ions despite collisions with the buffer gas.

The 1 m long flow tube had several finger inlets along the length for addition of neutral reactants. O_3 was added in known concentrations 59 cm prior to the end of the flow tube using the methods described below. Typical interaction times of ions with O_3 were 2.5 ms. The bulk of the gas flow is removed at the terminus of the flow tube using a Roots pump. The core of the flow was sampled through a 4-mm aperture in a rounded, carbon-coated nosecone and into a rough vacuum region. Ions were transported using a rectilinear quadrupole ion guide with asymmetric rods to a high vacuum region and the entrance of an orthogonally-accelerated time-of-flight Reflectron mass spectrometer (Jordan TOF Products). Ion abundances were monitored as a function of O_3 concentration using a detector comprised of three microchannel plates in a z-stack configuration operated in counting mode. Flight times were recorded using a time-to-digital convertor (ComTec 6TA1) and sent to a computer.

O_3 was generated using an Atlas Ozone Generator (Absolute Ozone) with 40 psig backing pressure of O_2 (Matheson, 99.997%). Experiments were conducted using the immediate output of the ozone generator (i.e., a mixture of O_2 and O_3), as described previously.[13] No clustering with O_2 was observed for any species and no exothermic bimolecular reactions with O_2 were identified for any ionic species observed. The O_3 concentration was determined by monitoring the absorption through an optical cell of 7.3 cm path length at either 248 nm or 290 nm using a UV spectrometer (STS-UV, Ocean Insight) with a deuterium/halogen light source (DH-mini, Ocean Insight). The pressure of the optical cell was monitored using a capacitance manometer (Instrutech) and the total gas flow metered up to 100 std. cm^3 min using a mass flowmeter (MKS Instruments). The ozone mixture was delivered to the flow tube through opaque PTFE tubing terminating in a ~5 cm long stainless-steel finger inlet.

Ca^+ injected into the flow tube encountered ~10^4 collisions with the helium buffer gas prior to addition of the ozone. For polyatomic species, this is a reliable method to ensure thermalization to the temperature of the flow tube walls; however, thermalization of a monatomic species is less certain. The ground state of Ca^+ is ^2S, with the lowest-lying excited states being ^2D levels about 1.7 eV higher in energy. The ^2D levels have radiative lifetimes of ~1s and could survive on the timescale of the experiment.[17] The experiment does not have direct detection of the Ca^+ state. Data were taken both with and without CO_2 present in the flow tube at $\sim 5\times10^{13}$ cm^{-3} as a quenchant. Because Ca^+ associates with CO_2 in a helium buffer under the present conditions at $\sim 5 \times 10^{-13}$ cm^3 s^{-1},[18] the polyatomic complex should allow for easier conversion of any ^2D to ^2S.[19] No differences in the data were observed with or without CO_2 present, except for the presence of $CaO_n^+(CO_2)$ cluster ions (Figures S2 and S3). Additionally, no differences in the data were seen as a function of source conditions or from day-to-day, which, from experience, is not consistent with the presence of excited state species affecting the reactivity. We conclude that either excited state Ca^+ is not present or that it is not measurably affecting the data.

Quantum chemical calculations

Calculations were performed using the Gaussian 16 quantum chemical software suite at the B3LYP/def2-TZVP level.[20] Minima and transition states along the various reaction coordinates were identified as containing exactly 0 or 1 imaginary frequency. Both doublet and quartet multiplicities were explored, with only doublet species found to be relevant at the energies here. Species were evaluated for wavefunction instability and spin-contamination. Transition states were confirmed to correlate to minima via intrinsic reaction coordinate (IRC) calculations. Reported energies are zero-point corrected.

Statistical modeling

The stochastic statistical modeling method applied here, which is based on the work of Troe and co-workers,[21–28] has been described in detail elsewhere.[29,30] For each reaction, a reaction coordinate defined by only the stationary points is determined using quantum chemical calculations. The specific rate constants $k(E,J)$, where E is internal energy and J is angular momentum, are calculated for each isomerization or dissociation along the reaction coordinate. Isomerization rate curves are calculated using Rice-Ramsperger-Kassel-Marcus (RRKM) theory.[31] Dissociation rate curves are calculated using the simplified statistical adiabatic channel model (SSACM),[32,33] a modified version of phase space theory (PST),[34] which can reproduce the results of the statistical adiabatic channel model (SACM).[35] In all cases, numbers and densities of states are calculated using the methods of Olzmann and Troe.[23,25]

A "trial" of the reaction from a set of initial conditions (defined by translational and vibrational energies, rotational energy and angular momentum, and impact parameter *b,* each selected randomly from thermal distributions) is evaluated to determine if a capture complex is formed. If the translational energy exceeds the long-range potential at a distance $r = b$, defined as:

$$V(r) = -q^2\alpha/2r^4 - q\,\mu_D \cos\Theta/r^2 + \hbar 2L(L+1)/2\mu_m r^2 \qquad (7)$$

where r is the distance between reactant centers of mass, q is the elementary charge, α is the isotropic polarizability of the neutral reactant, μ_D is the dipole moment of the neutral reactant, Θ is the angle between the dipole axis of the neutral and the line between the centers of mass at b, L is the orbital angular momentum, and μ_m is the reduced mass, then an entrance complex is formed. The value of Θ is treated in a manner described previously.[30] A capture rate constant can be derived as

$$k_{\text{capture}} = \pi \langle b \rangle^2 \langle \mathrm{v} \rangle, \tag{8}$$

where v is the reactant velocity, and can be compared to the Su-Chesnavich parameterized capture rate constant[36] for ion-dipole reactions.

The total energy of the complex is treated as the sum of translational, vibrational, and rotational energies, and full intramolecular vibrational energy redistribution (IVR) of the complex is assumed. The angular momentum of the complex is determined by summing the rotational and orbital angular momentum vectors. The reaction proceeds in a step-wise manner through either an isomerization, a dissociation, or a collision with the helium buffer gas with probabilities proportional to each calculated k(E,J). The effective unimolecular rate constant for helium collisions is determined from the number density in the experiment (typically 10^{16} cm^{-3}) and the LGS rate constant[9] (5.5×10^{-10} $\text{cm}^3\ \text{s}^{-1}$). On collisions with helium, internal energy of the complex is gained or lost as described previously.[37] The process is repeated until a dissociation occurs. Where of interest, the product energy distribution is calculated assuming phase space behavior according to the fragment ion, fragment neutral, and translational density of states.[38] The subsequent behavior (e.g., dissociation or stabilization) of the product ion fragment may be followed in a similar manner.

A sufficient number of trials are run in order to minimize random scatter in the events of interest, generally from 10^3-10^6 depending on the frequency of the event. The full calculation takes seconds to minutes using a desktop computer.

Results

Figure 1 shows representative data of measured ion abundances from an initial concentration of Ca^+ as a function of O_3 concentration after a fixed reaction time. 14 additional data sets under both quenched and unquenched conditions were collected and were consistent with that shown. The raw time-of-flight mass spectra are shown in Figure S1. The kinetics were modeled from the known initial conditions throughout the known reaction time by iteratively solving the coupled differential equations described by the possible chemistries occurring. The set of all exothermic reactions with O_3 as calculated at the B3LYP/def2-TZVP level (Table S2) was considered, and all rate constants varied in concert, limited by the calculated Su-Chesnavich capture rate constants. The resulting calculated ion abundances were compared to the data via a weighted least-squares difference.

Excellent fits to the data were found, and several rate constants and product branching fractions were well-constrained. Derived rate constants and uncertainties are shown in Table 1. Uncertainty in the rate constants is a convolution of the uncertainty in the fit along with systematic uncertainties of the experiment described previously.[16]

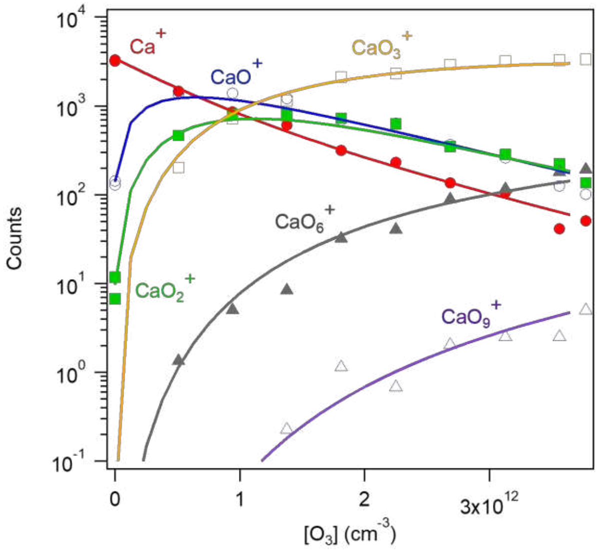

Figure 1. Counts of the indicated ions (Ca^+ red circles; CaO^+; blue open circles; CaO_2^+ green squares; CaO_3^+ orange open squares; CaO_6^+ grey triangles; CaO_9^+ purple open triangles) at 300 K and 0.35 Torr after 2.4 ms reaction time. Lines are modeled fits as described in the text.

Table 1. Derived (*k_{exp}*) and modeled room-temperature for $CaO_n^+ + O_3$ reactions and capture rate constants (*k_{cap}*) calculated using either the parameterization of Su and Chesnavich or the present statistical model (see text).[36]

		k ($cm^3\ s^{-1}$)		**k_{cap} ($cm^3\ s^{-1}$)**	
Reactants	**Products**	**k_{exp}**	**Stat Model**	**Su-Chesnavich**	**Stat Model**
$Ca^+ + O_3$	$CaO^+ + O_2$	$9.0 \pm 4 \times 10^{-10}$	1.1×10^{-9}	1.06×10^{-9}	1.07×10^{-9}
$CaO^+ + O_3$	total	$8.0 \pm 2 \times 10^{-10}$	1.0×10^{-9}	9.75×10^{-10}	9.95×10^{-10}
	$Ca^+ + 2O_2$	$2.0 \pm 1.5 \times 10^{-10}$	3.8×10^{-10}	-	-
	$CaO_2^+ + O_2$	$6.0 \pm 3 \times 10^{-10}$	4.1×10^{-10}	-	-
	$CaO_3^+ + O$	$1.5 \pm 0.7 \times 10^{-10}$	1.6×10^{-10}	-	-
$CaO_2^+ + O_3$	total	$9.0 \pm 3 \times 10^{-10}$	9.4×10^{-10}	9.24×10^{-10}	9.42×10^{-10}
	$CaO^+ + 2O_2$	$0.8 \pm 0.5 \times 10^{-10}$	5.2×10^{-10}	-	-
	$CaO_3^+ + O_2$	$8.0 \pm 3 \times 10^{-10}$	4.2×10^{-10}	-	-
$CaO_3^+ + O_3$	total	$2.0 \pm 1 \times 10^{-11}$	2.1×10^{-11}	8.90×10^{-10}	9.10×10^{-10}
	$CaO_2^+ + 2O_2$	$<2.0 \times 10^{-11}$	1.7×10^{-11}	-	-
	CaO_6^+	$1.0 \pm 0.5 \times 10^{-11}$ [a]	4×10^{-12}	-	-
$CaO_6^+ + O_3$	CaO_9^+	$1.0 \pm \times 2 \times 10^{-11}$ [a]	-	8.43×10^{-10}	

[a] Three-body process $CaO_n^+ + O_3 + He$ with effective two-body rate constant reported with $[He] = 1.1\times10^{16}\ cm^{-3}$.

The reaction sequence is visualized in Figure 2. The total rate constants of $CaO_n^+ + O_3$ are close to the calculated capture rate constant for n = 0 – 2. Oxidation of CaO_n^+ dominates for n = 1 – 2, comprising about 80% of reactions. Dissociative oxidation of CaO_n^+ by O_3 comprises the remainder of the CaO_2^+ reaction and much or all of the remainder of the CaO^+ reaction. Reaction of the type

$$CaO_n^+ + O_3 \rightarrow CaO_{n+2}^+ + O \quad (9)$$

may occur for n = 1. The only bimolecular reaction observed for n = 3 is dissociative oxidation, which occurs at a small fraction (~1%) of the calculated capture rate constant. n = 3 also clusters with O_3 to yield CaO_6^+, which clusters further to yield CaO_9^+.

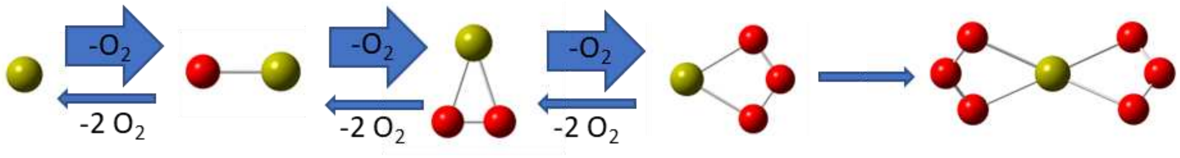

Figure 2. Representation of the reaction sequence initiated by $Ca^+ + O_3$. Arrows indicate reaction with O_3 at a rate constant corresponding to the thickness of the arrow, roughly 10^{-9} $cm^3\ s^{-1}$ (thick) or $<10^{-10}$ $cm^3\ s^{-1}$ (thin). Structures shown are the calculated lowest energy isomers.

The reformation of Ca^+ via dissociative oxidation of CaO^+ is of interest as it affects the determination of the $Ca^+ + O_3$ rate constant, which is of atmospheric interest. Ca^+ was converted to CaO^+ by addition of N_2O to the flow tube 50 cm prior to the reaction inlet, followed by reaction with O_3 as described above. The resulting data is sparse (Figure S4), but is well-modeled assuming the kinetics reported in Table 1 along with $Ca^+ + N_2O \rightarrow CaO^+ + N_2$ $k_{300} = 1.6 \times 10^{-10}$ $cm^3\ s^{-1}$ [39] and clearly shows formation of Ca^+.

Quantum calculation results of CaO_n^+ species are presented in Table S1. Little thermochemistry of these species is known experimentally. The Ca^+-O 0 K bond dissociation energy (BDE) has been measured at 3.57 ±0.05 eV[40] with the calculated value (3.35 eV) reasonably reproducing that number. Several isomers of CaO_2^+ are identified. The lowest energy is a superoxide species, i.e., $Ca^{2+}O_2^-$, with C_{2v} geometry. A linear $CaOO^+$ species lies about 1 eV higher in energy and another C_{2v} species with the O-O bond dissociated lies ~ 4 eV above the ground state. The lowest energy isomer of CaO_3^+ contains the geometry of the ozone anion and may be described as $Ca^{2+}(O_3^-)$. Several structures that may be described as $CaO^+(O_2)$ or $OCa^+(O_2)$ (i.e., a Ca-O bond length similar to CaO^+ and an O_2 bond length similar to neutral oxygen) are found ~0.75 eV higher in energy. No CaO_3^+ structure containing a superoxide O_2^- group could be identified. The lowest energy isomers of CaO_4^+ have the structure of ground state CaO_2^+ (i.e., $Ca^{2+}O_2^-$) coordinated to a neutral O_2 group; multiple minima differing in the orientation of the O_2 are found at similar energies. $Ca^+(O_2)_2$, i.e., two neutral O_2 groups coordinated to Ca^+, lies about 1 eV higher in energy. $CaO^+(O_3)$ and a structure with an O_2 group coordinated to the higher energy CaO_2^+ C_{2v} structure lie about 2.5 eV and 3 eV above the ground state, respectively. Higher oxides were explored less exhaustively. For CaO_5^+, a structure corresponding to ozone coordinated to ground state $Ca^{2+}O_2^-$ is identified. For CaO_6^+, a structure that may be described as $Ca^+(O_3)_2$ is identified. Calculated reaction coordinates for each reaction are discussed below.

Discussion

$Ca^+ + O_3$

The rate constant of $Ca^+ + O_3$ is of atmospheric interest for models of Ca^+ and Ca concentrations in the mesosphere and lower thermosphere.[6] Several previous measurements[8,14,15] have indicated a rate constant of one half or less of the calculated capture rate constant. However, several similarly slow measurements of bare metal cations with ozone have been shown to be spurious due to analyses not accounting for reforming of the primary cation through sequential ozone chemistry.[10–12] Here we report a larger rate constant (Table 1), near the calculated capture rate constant.

The present SIFT, previous SIFT,[14] and previous flowing afterglow[8] data all show subtle curvature in the Ca^+ decay, consistent with reaction 5b (dissociative oxidation of CaO^+) occurring. The present and prior SIFT raw data are in reasonably good agreement (Figure S7), differing somewhat in the CaO^+ and CaO_2^+ abundances at large extent of reaction. Quantitative comparison is limited as the prior SIFT data shows a doubling of the total ion counts at large extent of reaction, indicating significant mass discrimination. Still, it appears that the data are in agreement and the different reported rate constants are not due to an artifact of one experiment or the other. Instead, the difference in the reported rate constants hinges on the contribution of reaction 5b, $CaO^+ + O_3 \rightarrow Ca^+ + 2O_2$ to reform Ca^+.

Analysis of the present data excluding reaction 5b (Figure S6) provides a marginal fit to the experimental data with a $Ca^+ + O_3$ rate constant of 5×10^{-10} cm^3 s^{-1}, similar to the previously reported values. The fit is a compromise, overestimating the abundance of Ca^+ at small extent of reaction while underestimating it at large extent of reaction. The observed curvature in the Ca^+ is better fit assuming reforming of Ca^+ via reaction 5b (Figure 1). Reaction initiated by CaO^+ with no Ca^+ initially present (Figure S4) shows an increase in Ca^+ consistent with the kinetics reported in Table 1, confirming that reaction 5b occurs. From the flow tube data, it appears most likely that reaction 5b is occurring at between 1 - 4 $\times 10^{-10}$ cm^3 s^{-1}.

The LIF data shows a clear single exponential decay of Ca^+; however, the experiment is insensitive to the smallest extents of reaction due to a settling time of ~60 ns after Ca^+ production via laser ablation.[15] This leads to an unfortunate ambiguity in that the initial concentration of Ca^+ may be larger than extrapolated, and curvature in the decay hidden in that settling time (Figure S8). The data may be modeled with $Ca^+ + O_3$ rate constants as large as 8×10^{-10} cm^3 s^{-1} (or larger if $k_{5b} > 4 \times 10^{-10}$ cm^3 s^{-1}).

There remains some uncertainty in the $Ca^+ + O_3$ rate constant, although it is likely larger than the literature values by up to about a factor of 2. Considering the present and prior data, we suggest a value of $8 \pm 3 \times 10^{-10}$ cm^3 s^{-1}. In the most recent model of Ca and Ca^+ behavior in the mesosphere,[6] a value of 3.9 $\times 10^{-10}$ cm^3 s^{-1} was initially assumed. The model failed to reproduce certain seasonal features of the Ca concentrations measured using lidar. An adjusted model in which a capture rate constant of 1.1×10^{-9} cm^3 s^{-1} was used reproduced those seasonal features, but led to overestimation of the total Ca concentration.

The calculated reaction coordinate (Figure 3) is somewhat trivial. A $Ca^+(O_3)$ entrance complex is formed with a large amount of internal excitation. Statistical assumptions suggest a rapid isomerization and dissociation (the lowest energy pathway identified is shown in Figure 2, with more details shown in Figure S9). The expected lifetime of the $Ca^{2+}(O_3^-)$ intermediate to dissociation to $CaO^+ + O_2$ is sub-picosecond and IVR must be incomplete making a statistical analysis improper. Still, this dissociation must dominate over dissociation back to $Ca^+ + O_3$ reactant. As such, the modeling predicts a capture-controlled reaction with a rate constant essentially equal to the Su-Chesnavich capture rate constant (Table 1).

The reaction

$$Ca^+ + O_3 \rightarrow CaO_2^+ + O \tag{10}$$

is calculated to be ~1.5 eV exothermic. However, no reaction pathway from the $Ca^+(O_3)$ entrance complex was identified from the density functional calculations. A more direct reaction may be possible, but $CaO^+ + O_2$ is energetically preferred. Modeling the SIFT data shown in Figure 1 suggests that reaction 10 could be occurring at a rate constant of up to ~10^{-10} cm^3 s^{-1}.

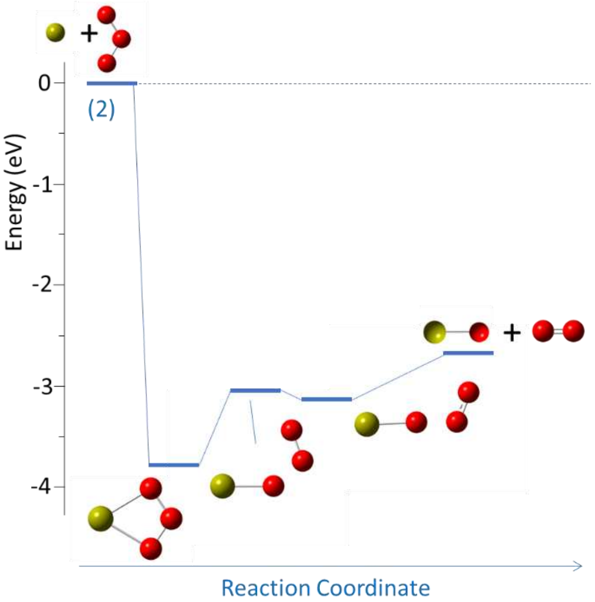

Figure 3. Reaction coordinate of $Ca^+ + O_3$ calculated at the B3LYP/def2-TZVP level.

$CaO^+ + O_3$

The kinetics of $CaO^+ + O_3$, and of the other higher oxides, are likely of less mesospheric relevance. The mesospheric concentration of O_3 is ~10^7 cm^{-3}, far below that of oxygen atoms at ~10^{11} cm^{-3}.[41] As such, the reaction cannot compete with reaction with oxygen atoms

$$CaO^+ + O \rightarrow Ca^+ + O_2 \tag{11}$$

which proceeds with a rate constant[42] of 4.2 ±2.8 ×10^{-11} cm^3 s^{-1} and dissociative recombination with electrons

$$CaO^+ + e^- \rightarrow Ca + O \tag{12}$$

which proceeds with a rate constant of 3±1 ×10^{-7} cm^3 s^{-1}.[43] However, the mechanism of the reaction is more interesting, particularly the competition between reactions 5a and 5b. The calculated reaction coordinate appears in Figure 4. The entrance $CaO(O_3)^+$ complex is bound by ~1 eV relative to reactants, much less than is Ca^+-O_3 at almost 4 eV. The Ca atom again has a 2+ partial charge, but the negative charge is distributed between the lone oxygen atom and the O_3 group. The resulting Ca-O bond is longer than in CaO^+ and the bond distances in the O_3 in between the O_3 and O_3^- bond distances. The entrance complex can dissociate to $CaO_3^+ + O$ or isomerize to $CaO_2^+(O_2)$. The potential surface around the isomerization is complex with a number of minimally separated intermediates. We were unable to identify the transition state to $CaO_2^+(O_2)$, but believe it is likely not a substantial barrier. The CaO_2^+-(O_2) bond is weak (~0.5 eV) and dissociation will occur rapidly to yield $Ca^{2+}(O_2^-) + O_2$. If the ionic product has more than ~ 2 eV of internal excitation, further dissociation to $Ca^+ + O_2$ will occur rapidly.

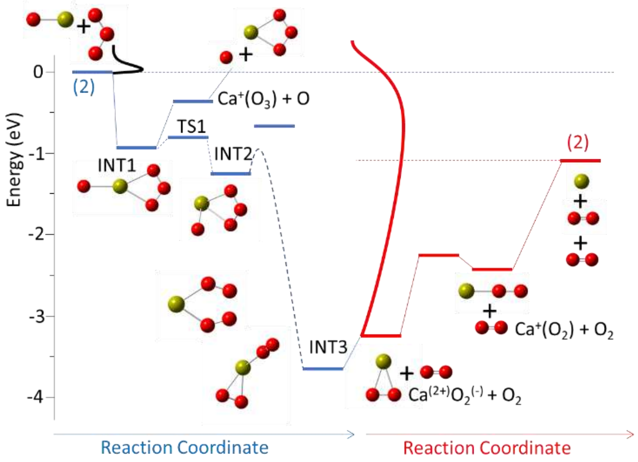

Figure 4. Reaction coordinates of $CaO^+ + O_3$ (blue) and CaO_2^{+*} (red) calculated at the B3LYP/def2-TZVP level. Initial internal energy distributions of the reactants (black) and CaO_2^+ product (red) as calculated using the statistical modeling (see text) are shown.

Assuming a statistical product energy distribution for the dissociation $Ca^{2+}(O_2^-)$-$(O_2) \rightarrow Ca^{2+}(O_2^-) + O_2$ (Figure 5) somewhat overestimates the fraction of Ca^+ produced relative to the experiment (Table 1). This is perhaps not surprising as the rate curve for the reaction assuming statistical behavior suggests a sub-picosecond dissociation and IVR is likely incomplete. The data indicate that the prompt dissociation results in less internal excitation of the $Ca^{2+}(O_2^-)$ product than the statistical distribution.

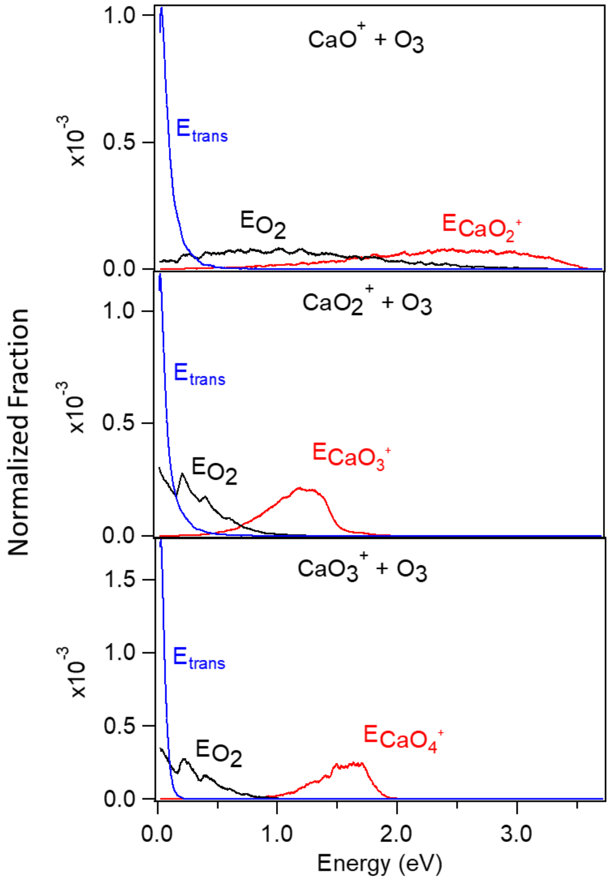

Figure 5. Calculated product energy distributions for the dissociation of CaO_{n+1}^+-O_2 initiated by the indicated reactions. As labeled, product translational energy (E_{trans}, blue curve), O_2 neutral internal energy (E_{O2}, black curve), CaO_{n+1}^+ internal energy (E_{CaO4+}, red curve).

CaO_2^+ + O_3

The CaO_2^+ + O_3 reaction is observed to react near the capture rate producing mostly CaO_3^+ along with a minority of CaO^+ (Table 1). The calculated reaction coordinate for CaO_2^+ + O_3 appears in Figure 6. The entrance complex is best described as $Ca^{2+}(O_3^-)(O_2)$ with the negative charge fully on the O_3 group, leading to a stronger Ca-O_3 bond and a weaker Ca-O_2 bond. The mechanism appears analogous to that for CaO^+ + O_3. The entrance complex can rapidly dissociate to $Ca^{2+}(O_3^-)$ + O_2. When the $Ca^{2+}(O_3^-)$ product is formed with more than ~1 eV internal energy, further dissociation to yield CaO^+ occurs. Again, the statistical model overestimates the fraction of dissociative oxidation relative to the experiment. However, here the dissociation is not clearly non-statistical, occurring with a rate constant of ~10^{11} s^{-1}. From the calculated product energy distribution (Figures 5,7) the data would be explained with a reasonable adjustment (~0.15 eV) to the calculated energy of CaO^+ + $2O_2$ relative to reactants.

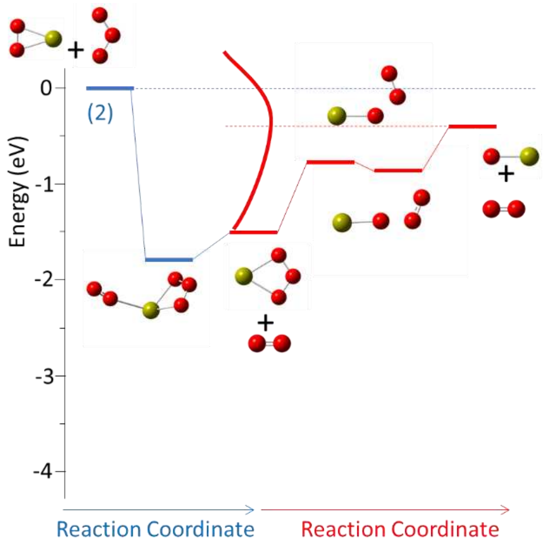

Figure 6. Reaction coordinates of CaO_2^+ + O_3 (blue) and CaO_3^{+*} (red) calculated at the B3LYP/def2-TZVP level. Initial internal energy distribution CaO_3^+ product (red curve) as calculated using the statistical modeling (see text) is shown.

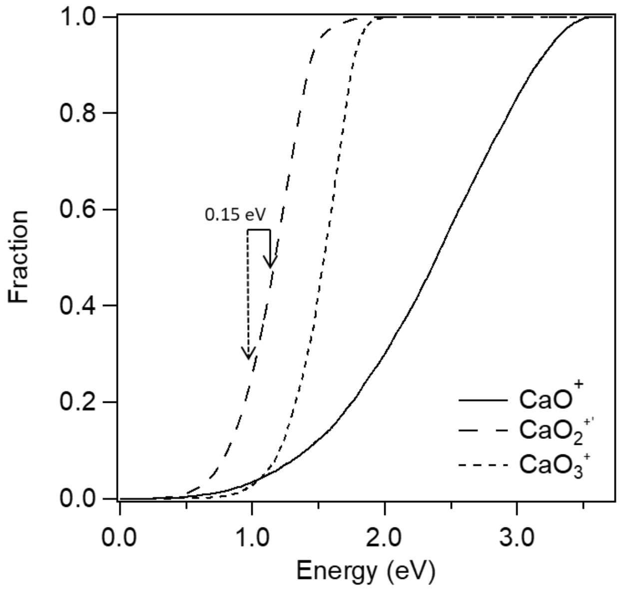

Figure 7. Calculated fraction of CaO_{n+1}^+ product ions with at least the internal energy indicated than from CaO_n^+ + O_3 (n=1 solid curve, n=2 large dashed curve, n=3 small dashed curve). Solid arrow indicates the calculated threshold for dissociative oxidation in the CaO_2^+ + O_3 reaction while the dashed arrow indicates the threshold required to fit the experimental data.

CaO_3^+ + O_3

The $CaO_3^+ + O_3$ reaction is distinct from the CaO^+ and CaO_2^+ reactions. The reaction proceeds at only a small fraction (~2%) of the capture rate. No oxidation product (CaO_4^+) is observed. Instead, both a dissociative oxidation product (CaO_2^+) and an association product (CaO_6^+) are seen. The calculated reaction coordinate appears in Figure 8. Analogous to the $OCa(O_3)^+$ complex, the CaO_6^+ species has a 2+ charge on the Ca atom and a negative charge distributed between the two O_3 groups, leading to weaker bond energies. Unlike the other reactions discussed, a barely submerged (i.e., slightly below the energy of the separated reactants) isomerization barrier exists. As a result, most CaO_6^+ complexes formed dissociate back to reactants resulting in the observed small reaction efficiency. A small fraction of the CaO_6^+ complexes are collisionally stabilized. The pressure dependence of the process was not investigated and an effective 2-body rate constant is reported in Table 1. Likely, this measurement is in the region of linear pressure dependence and corresponds to a termolecular rate constant of 1×10^{-27} cm^3 s^{-1}. Reactions that do proceed undergo isomerization to $Ca^+(O_2)_2$, which is extremely weakly bound and always dissociates to yield the observed CaO_2^+ product. At the calculated energetics a very small fraction (partial rate constant ~10^{-13} cm^3 s^{-1}) are predicted to retain sufficient energy to dissociate further to yield Ca^+. The uncertainty in the energetics creates a large uncertainty in this partial rate constant and it is not clear from the experimental data whether or not the channel contributes.

We note that this suggests a catalytic cycle of ozone destruction (either $Ca^+ + 2O_3 \rightarrow Ca^+ + 6O_2$ or $CaO_2^+ + 2O_3 \rightarrow CaO_2^+ + 6O_2$); however, because the polyatomic CaO_n^+ species have a short lifetime to reaction with oxygen atoms,[42] this should not be a major source of O_3 destruction. We have suggested previously for the reactions[13] of $NdO_2^+ + O_3$ and $SmO_2^+ + O_3$ that a mechanism best described as a direct oxidation of O_3 could be occurring. This reaction is analogous to those as the termination step of the $MO_n^+ + O_3$ cycle. From the calculated reaction coordinate, in this case the mechanism is again a dissociative oxidation of CaO_3^+, not an oxidation of O_3.

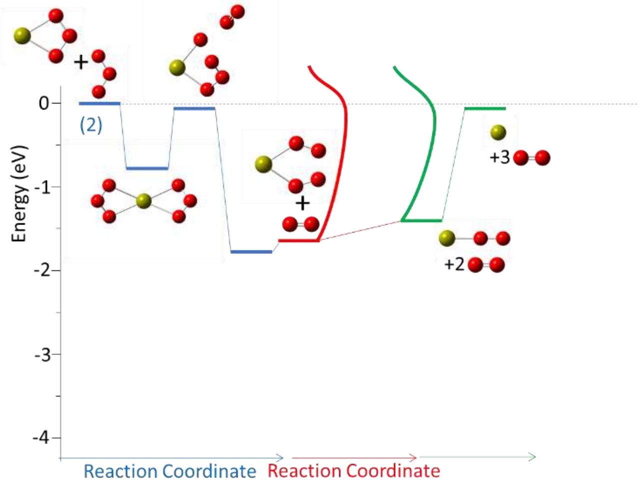

Figure 8. Reaction coordinates of $CaO_3^+ + O_3$ (blue), CaO_4^{+*} (red), and CaO_2^{+*} (green) calculated at the B3LYP/def2-TZVP level. Initial internal energy distributions of the CaO_4^+ (red), and CaO_2^+ (green) products as calculated using the statistical modeling (see text) are shown.

A comparison of the statistical modeled rate constants and the experimental data appears in Figure 9. In all cases, the total rate constants are well-reproduced, with the $CaO_n^+ + O_3$ $n \leq 2$ reactions being capture controlled and the $CaO_3^+ + O_3$ reaction occurring with about 2% efficiency under the present conditions. The product branching fractions for the $CaO^+ + O_3$ and $CaO_2^+ + O_3$ reactions are marginally reproduced; in both cases the statistical model overestimates the partial rate constants for dissociative oxidation to $CaO_{n-1}^+ + 2O_2$. The relevant dissociation of CaO_4^{+*} in the CaO^+ reaction likely occurs too quickly for IVR to be complete, and the statistical product energy distribution is not expected. The relevant dissociation of CaO_5^+ in the $CaO_2^+ + O_3$ reaction is more likely to occur statistically, but the modeled product branching is extremely sensitive to the calculated energetics, with the values needed to reproduce the experimental product branching within the uncertainty of the calculations.

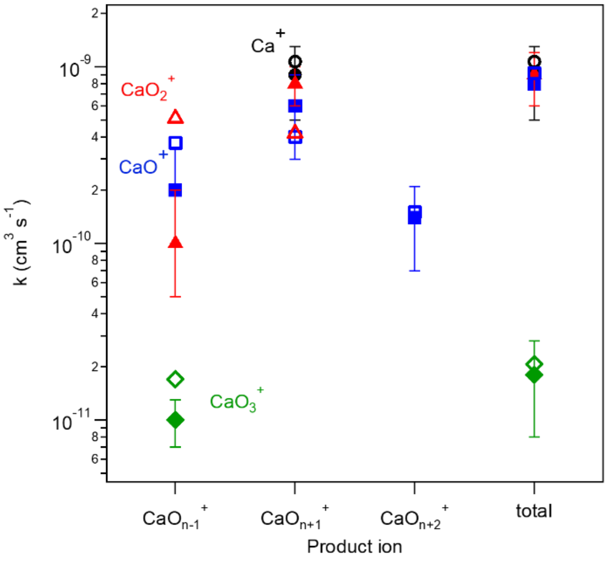

Figure 9. Comparison of experiment (solid points) and statistical model (open points) total and partial rate constants for $CaO_n^+ + O_3$ (n=0 (black circles), 1 (blue squares), 2 (red triangles), 3 (green diamonds) yielding products either $CaO_{n-1}^+ + 2\ O_2$, $CaO_{n+1}^+ + O_2$, or $CaO_{n+2} + O$.

Implications for Ca chemistry in the mesosphere and lower thermosphere

To explore the impact of these results on Ca species in the mesosphere and lower thermosphere (MLT), we used a global model with a full treatment of the neutral and ion-molecule chemistry of calcium injected into the upper atmosphere by meteoric ablation. The first version of this model[6] used the Whole Atmosphere Community Climate Model (WACCM) within the Community Earth System Model (CESM) developed by the National Center for Atmospheric Research (Boulder, CO). WACCM is a coupled chemistry-climate model that extends from the Earth's surface to the lower thermosphere (~140 km), with 88 vertical model levels giving a resolution of ~3.5 km in the upper mesosphere/lower thermosphere region. For the present study we employed WACCM version 6, within the framework developed from the second iteration of the fully coupled CESM2.[44] To reduce computational cost, we used free-running WACCM6 simulations at 1.9° latitude × 2.5° longitude horizontal resolution, under Year 2000 conditions, with repeating Year 2000 climatological sea surface temperatures, greenhouse gases, aerosol and solar forcing input, and present day emissions from the Coupled Model Intercomparison Project Phase 6 (CMIP6).[45]

Table S1 in the SI lists the full set of neutral and ion-molecule reactions involving calcium species. The objective was to examine the impact from the increased rate coefficient for the reaction between Ca^+ and O_3 (reaction 1, R25 in Table S3), and the additional Ca oxide ion chemistry (R27, R29 and R30 in Table S3) from the present study. For the reaction between CaO_3^+ and O_3, we have not included the addition channel forming CaO_6^+, since this should not compete under the low pressure conditions of the MLT with the bimolecular channel (R30). Since CaO_3^+ is a new species in WACCM-Ca, we then added the reaction $CaO_3^+ + O \rightarrow CaO_2^+ + O_2$ (R32) with a rate coefficient set to that of the analogous reaction $CaO_2^+ + O$;[42] and the dissociative recombination of CaO_3^+ with an electron (R41), which we assume proceeds via the most exothermic channel to $CaO + O_2$, and assigned the rate coefficient to be the same as that for CaO^+.[43]

Three WACCM-Ca simulations were carried out: the first run used the Ca chemistry reaction set from ref. [6]; the second run was identical except that k_1 (k_{25} in Table S1) was increased from 3.9×10^{-10} cm^3 s^{-1} to the new value of 9×10^{-10} cm^3 s^{-1} (Table 1); and the third run contains the complete new Ca chemistry module in Table S1. All these simulations used the same injection rate of meteoric Ca as a function of latitude and month.[6] Model output was sampled every 30 minutes at the following locations: lidar stations at Kühlungsborn (54°N, 22°E) and Arecibo (18°N, 293°E) with extensive measurements of Ca and Ca^+; and rocket launching sites at Kiruna, Sweden (68°N, 22°E), Redlake, Canada (51°N, 267°E) and Wallops, Virginia, U.S. (38°N, 285°E) where Ca^+ ions have been measured by mass spectrometry.[6]

Each model simulation was run for 4 years to establish year-to-year consistency. The model output in the fourth year is discussed here. Figure 10 shows the mean midday and midnight profiles of Ca, Ca^+ and the major molecular ions (concentrations > 0.01 cm^{-3}) during August, at Kühlungsborn (54°N, 22°E). This mid-latitude location is the site of the Institute of Atmospheric Physics, where a multi-year set of Ca measurements were performed using the resonance lidar technique.[6,46] In comparison with the original Ca chemistry (black lines), the increased rate coefficient for $Ca^+ + O_3$ (red lines) and the inclusion of all the new Ca oxide ion chemistry (green lines) leads to a faster overall rate of neutralisation of Ca^+ to Ca, so that Ca^+ decreases and Ca increases between 85 and 105 km. The inclusion of the additional chemistry and the new species CaO_3^+ has a small effect on Ca and Ca^+ above 80 km where the latter species dominate. However, below 80 km there are larger relative changes, but the absolute concentrations are all small (< 1 cm^{-3}) and so not measurable by mass spectrometry on rockets where detection limits are usually above 10 cm^{-3}.[47,48]

Figure 10 shows that Ca^+, which is the major calcium species above 80 km, exhibits little diurnal variation. In contrast, the Ca oxide ions increase significantly at night: in particular, CaO_3^+ increases by a factor of nearly 100 from a midday peak concentration of 10^{-3} to a layer peaking close to 0.1 cm^{-3} at midnight (Figure 10b). The reason for this is that below 84 km the atomic O concentration decreases significantly at night through removal by recombination with O_2,[1] so that the reactions of the Ca oxide ions with O (R26, R31 and R32 in Table S3) become much slower than in the day. In addition, the electron density decreases by around 1 order of magnitude as the molecular ions NO^+ and O_2^+ are rapidly removed by dissociative recombination,[1] which slows the neutralization of the Ca oxide ions. The rate of ionization of Ca through charge transfer with NO^+ and O_2^+, and also by photo-ionization (Table S3) is also effectively switched off at night, leading to the larger nighttime concentrations of atomic Ca between 90 and 110 km.

Figure 11a illustrates the monthly average vertical profiles of the atomic Ca concentration at 54°N, 22°E, where the lidar measurements were made.[46] Since these are night-time only measurements, the other panels in Figure 11 show the results of the three WACCM-Ca simulations averaging only night-time data. This figure demonstrates good agreement between the observations and all three simulations regarding the layer peak altitude (~87 km), the layer vertical extent (~84 – 96 km), and the pronounced minimum during northern hemisphere spring. However, the 51% increase in the autumnal Ca peak density (cf. Fig. 11(d) with (b)) is in significantly better agreement with the observations (Fig. 11(a)). This demonstrates the impact of the enhanced rate of neutralization of Ca^+ through reactions with O_3 producing a range of oxide ions which then undergo dissociative recombination with electrons.

The corresponding monthly average night-time vertical profiles of Ca^+ are shown in Figure S11 for the three WACCM-Ca simulations. The peak of the Ca^+ layer is ~3 km higher than that of the Ca layer. Although the Ca^+ layer also exhibits a spring-time minimum, the maximum in the peak density occurs in mid- to late summer, which reflects the longer daylight hours when Ca^+ is produced from Ca both by direct photo-ionization and charge transfer with ambient NO^+ and O_2^+ ions. Although rocket-borne mass spectrometric and lidar measurements of Ca^+ are available, Ca^+ densities are much more variable than neutral Ca (see, e.g., Figure 4a in [6]), so that comparison with the model simulations of Ca^+ is less useful.

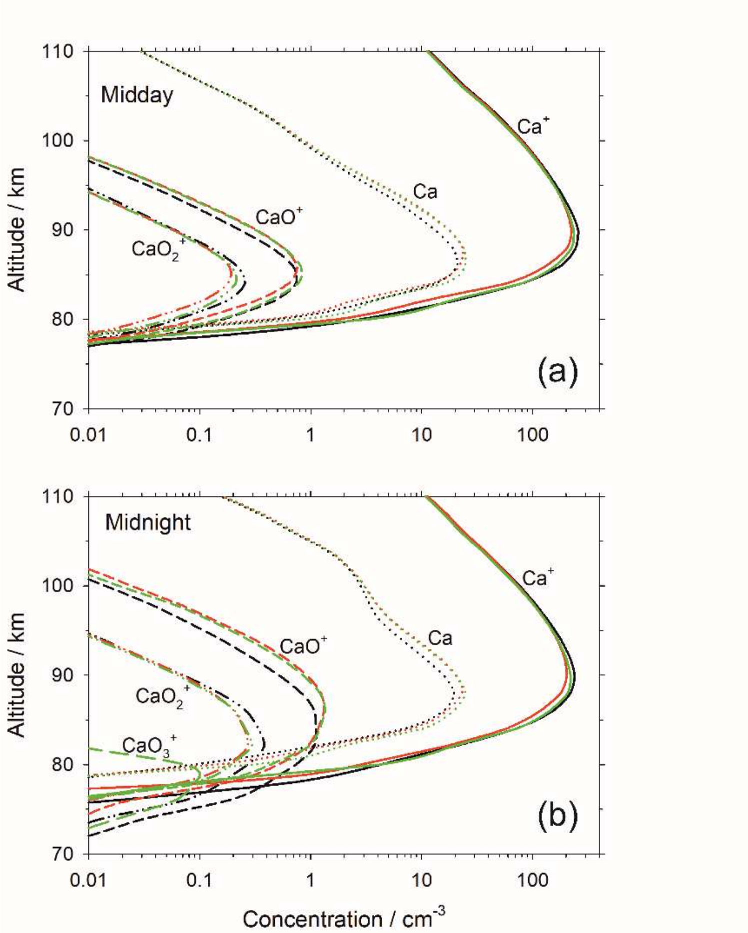

Figure 10. Modeled vertical profiles of Ca, Ca^+ and the major molecular ions between 70 and 110 km for August at 54ºN, 22ºE using Ca chemistry from Ref. [6] (black lines), with $k_1(Ca^+ + O_3)$ changed to that of the present study (red lines), and the WACCM-Ca model updated with all the new chemistry from the present study: (a) midday and (b) midnight.

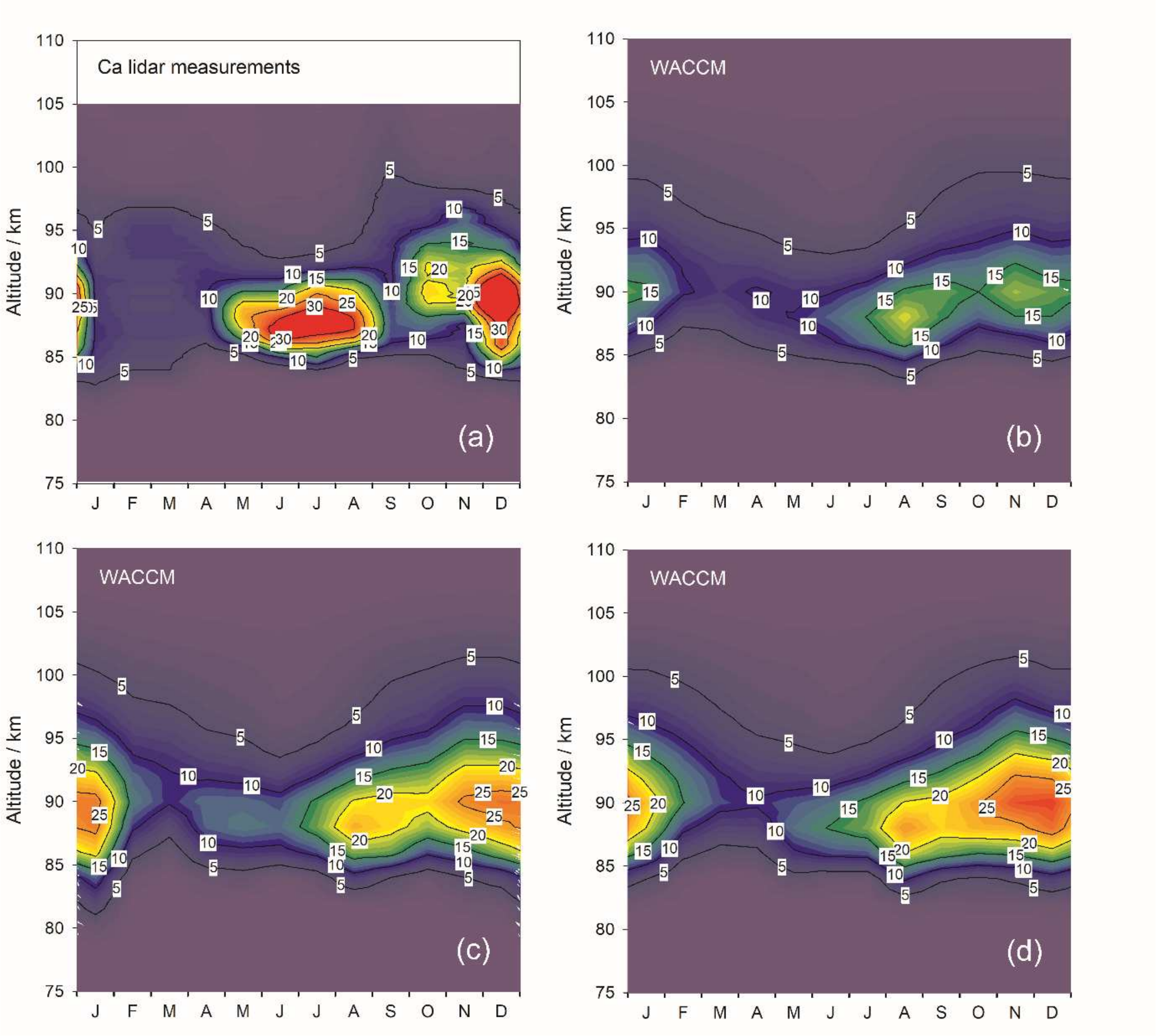

Figure 11. Monthly average night-time vertical profiles of Ca concentration (atom cm^{-3}) at 54°N, 22°E: (a) lidar measurements of Ca made at the Institute for Atmospheric Physics, Kühlungsborn;[6] (b) WACCM-Ca model with Ca chemistry from; (c) WACCM-Ca model with the rate coefficient for R25 (Ca$^+$ + O$_3$) changed to that of the present study; (d) WACCM-Ca model updated with all the new chemistry from the present study.

Conclusion

The kinetics of CaO_n^+ (n = 0-3) + O_3 have been measured using a selected-ion flow tube apparatus at 300 K. The $Ca^+ + O_3$ rate constant has been reported several times at between $1 – 4 \times 10^{-10}$ $cm^3\ s^{-1}$.[8,14,15] Here a larger value of $9 \pm 4 \times 10^{-10}$ $cm^3\ s^{-1}$ is derived. It appears likely, but not definite, that earlier analyses did not fully account for reformation of Ca^+ through sequential chemistry, resulting in an artificially small rate constant. A recommended value of $8 \pm 3 \times 10^{-10}$ $cm^3\ s^{-1}$ is consistent with the reported data from all of the present and previous experiments. The updated rate constant may be incorporated into models of atmospheric calcium,[6] which are important as a convenient proxy for all meteoric metal concentrations.

Higher oxides n = 1 and n = 2 produce both CaO_{n+1}^+ oxidized product and CaO_{n-1}^+ reduced product. The data here support a dissociative oxidation mechanism leading to the reduced product. O_3 oxidized CaO_n^+ to CaO_{n+1}^{+*} with a broad internal energy distribution. When there is sufficient energy, CaO_{n+1}^{+*} dissociates to $CaO_{n-1}^+ + O_2$, while when internal energy is lower, it is stabilized to CaO_{n+1}^+. The result is a complex cycle of $CaO_n^+ + O_3$ reactions, terminating at CaO_3^+, which only undergoes dissociative oxidation as CaO_4^+ is very weakly bound to O_2-loss. The cycle results in catalytic conversion of O_3 to O_2.

Ca and Ca^+ concentrations were calculated as a function of day-of-year, latitude, and altitude using the WACCM6 chemistry-climate model. Monthly-averaged vertical profiles of Ca concentrations were compared to lidar measurements at 54°N, 22°E (Kühlungsborn). Improved agreement in seasonal variation is found when using the elevated $Ca^+ + O_3$ rate constant reported here as compared to the lower literature value. Additional minor changes in the modeled ion and neutral concentrations are seen when using the full set of calcium oxide ion rate constants reported here.

Acknowledgements

The views expressed are those of the authors and do not reflect the official guidance or position of the United States Government, the Department of Defense, or of the United States Air Force. This work was supported by the Air Force Office of Scientific Research under AFOSR-22RVCOR009 (AFRL). BCS was supported through the Institute for Scientific Research of Boston College under contract FA9453-10-C-0206. AL received support through the AFRL Scholars program and by the Air Force Office of Scientific Research under AFOSR award No. FA9550-18-1-0213. JMCP and WF were supported by the European Research Council (project 291332 - CODITA) and the European Office of Aerospace Research and Development (award no. FA8655-21-1-7031). The three WACCM-Ca models and output are archived in the Petabyte Environmental Tape Archive and Library at the University of Leeds via https://petal.leeds.ac.uk/.

References

(1) Plane, J. M. C. The Mesosphere and Metals: Chemistry and Changes. *Chem. Rev.* **2015**, *115*, 4497–4541.

(2) Plane, J. M. C. Atmospheric Chemistry of Meteoric Metals. *Chem. Rev.* **2003**, *103*, 4963–4984.

(3) Haldoupis, C. Midlatitude Sporadic E. A Typical Paradigm of Atmosphere-Ionosphere Coupling. *Sp. Sci. Rev.* **2012**, *168*, 441–461.

(4) Raizada1, S.; Smith, J. A.; Lautenbach, J.; Aponte, N.; Perillat, P.; Sulzer, M.; Mathews, J. D. New Lidar Observations of Ca+in the Mesosphere and Lower Thermosphere Over Arecibo. *Geophys. Res. Lett.* **2020**, *47*, L087113.

(5) Jiao, J.; Chu, X.; Wang, H. J. Z.; Xun, Y.; Du, L.; Zheng, H.; Wu, F.; Xu, J.; Yuan, W.; Yan, C.; Wang, J.; Yang, G. First Lidar Profiling of Meteoric Ca^+ Ion Transport From ~80 to 300 Km in the Midlatitude Nighttime Ionosphere. *Geophys. Res. Lett.* **2022**, *49*, e2022gl100537.

(6) Plane, J. M. C.; Feng, W.; Juan Carlos Gómez Martín; Gerding, M.; Raizada, S. A New Model of Meteoric Calcium in the Mesosphere and Lower Thermosphere. *Atmos. Chem. Phys.* **2018**, *18*, 14799–14811.

(7) Ruscic, B.; Bross, D. H. *Active Thermochemical Tables (ATcT) based on ver. 1.122r of the Thermochemical Network (2021); available at ATcT.anl.gov*. https://atct.anl.gov.

(8) Ferguson, E. E.; Fehsenfeld, F. C. Some Aspects of Metal Ion Chemistry of the Earth's Atmosphere. *J. Geophys. Res.* **1968**, *73* (19), 6215. https://doi.org/10.1029/JA073i019p06215.

(9) Gioumousis, G.; Stevenson, D. P. Reactions of Gaseous Molecule Ions with Gaseous Molecules. V. Theory. *J. Chem. Phys.* **1958**, *29* (2), 294–299. https://doi.org/10.1063/1.1744477.

(10) Melko, J. J.; Ard, S. G.; Le, T.; Miller, G. S.; Martinez, O.; Shuman, N. S.; Viggiano, A. A. Determining Rate Constants and Mechanisms for Sequential Reactions of Fe^+ with Ozone at 500 K. *J. Phys. Chem. A* **2017**, *121* (1), 24–30.

(11) Rowe, B. R.; Fahey, D. W.; Ferguson, E. E.; Fehsenfeld, F. C. Flowing Afterflow Studies of Gas Phase Magnesium Ion Chemistry. *J. Chem. Phys.* **1981**, *75*, 3325–3328.

(12) McDonald, D. C.; Sweeny, B. C.; Ard, S. G.; Melko, J. J.; Ruliffson, J. E.; White, M. C.; Viggiano, A. A.; Shuman, N. S. Temperature and Isotope Dependent Kinetics of Nickel-Catalyzed Oxidation of Methane by Ozone. *J. Phys. Chem. A* **2018**, *122* (33), 6655–6662. https://doi.org/10.1021/acs.jpca.8b02513.

(13) Sweeny, B. C.; Heaven, M. C.; Lachowicz, A.; Johnson, M. A.; Viggiano, A. A.; Shuman, N. S.; Ard, S. G. Gas-Phase Reactivity of Ozone with Lanthanide Ions (Sm^+, Nd^+) and Their Higher Oxides. *J. Am. Soc. Mass Spectrom.* **2022**, *in press*. https://doi.org/10.1021/jasms.2c00058.

(14) Feil, S.; Koyanagi, G. K.; Viggiano, A. A.; Bohme, D. K. Ozone Reactions with Alkaline-Earth Metal Cations and Dications in the Gas Phase: Room-Temperature Kinetics and Catalysis. *J. Phys. Chem. A* **2007**, *111* (51), 13397–13402. https://doi.org/10.1021/jp076855g.

(15) Broadley, S. L.; Vondrak, T.; Plane, J. M. C. A Kinetic Study of the Reactions of Ca^+ Ions with O_3, O_2, N_2, CO_2, and H_2O. *Phys. Chem. Chem. Phys* **2007**, *9*, 4357–4369.

(16) Sweeny, B. C.; Ard, S. G.; Viggiano, A. A.; Shuman, N. S. Reaction of Mass-Selected, Thermalized $V_nO_m^+$ Clusters with CCl_4. *J. Phys. Chem. A* **2019**, *123*, 4817–4824.

(17) Kreuter, A.; Becher, C.; Lancaster, G. P. T.; Mundt, A. B.; Russo, C.; Häffner, H.; Roos, C.; Hänsel, W.; Schmidt-Kaler, F.; Blatt, R.; Safronova, M. S. Experimental and Theoretical Study of the 3d ^{2}D Level Lifetimes of $^{40}Ca^+$. *Phys. Rev. A* **2005**, *71*, 032504.

(18) Bohme, D. K.; Koyanagi, G. K. Gas-Phase Reactions of Carbon Dioxide with Atomic Transition-Metal and Main-Group Cations: Room-Temperature Kinetics and Periodicities in Reactivity. *J. Phys. Chem. A* **2006**, *110*, 1232–1241.

(19) Ferguson, E. E. Vibrational Quenching of Small Molecular Ions in Neutral Collisions. *J. Phys. Chem.* **1986**, *90*, 731–738.

(20) Frisch, M. J.; Trucks, G. W.; Schlegel, H. B.; Scuseria, G. E.; Robb, M. A.; Cheeseman, J. R.; Scalmani, G.; Barone, V.; Petersson, G. A.; Nakatsuji, H.; Li, X.; Caricato, M.; Marenich, A. V; Bloino, J.; Janesko, B. G.; Gomperts, R.; Mennucci, B.; Hratchian, H. P.; Ortiz, J. V; Izmaylov, A. F.; Sonnenberg, J. L.; Williams-Young, D.; Ding, F.; Lipparini, F.; Egidi, F.; Goings, J.; Peng, B.; Petrone, A.; Henderson, T.; Ranasinghe, D.; Zakrzewski, V. G.; Gao, J.; Rega, N.; Zheng, G.; Liang, W.; Hada, M.; Ehara, M.; Toyota, K.; Fukuda, R.; Hasegawa, J.; Ishida, M.; Nakajima, T.; Honda, Y.; Kitao, O.; Nakai, H.; Vreven, T.; Throssell, K.; Montgomery Jr., J. A.; Peralta, J. E.; Ogliaro, F.; Bearpark, M. J.; Heyd, J. J.; Brothers, E. N.; Kudin, K. N.; Staroverov, V. N.; Keith, T. A.; Kobayashi, R.; Normand, J.; Raghavachari, K.; Rendell, A. P.; Burant, J. C.; Iyengar, S. S.; Tomasi, J.; Cossi, M.; Millam, J. M.; Klene, M.; Adamo, C.; Cammi, R.; Ochterski, J. W.; Martin, R. L.; Morokuma, K.; Farkas, O.; Foresman, J. B.; Fox, D. J. Gaussian 16 . C.01. Gaussian Inc.: Wallingford, CT 2016.

(21) Troe, J. Specific Rigidity Factors in Simple Unimolecular Bond Fission Reactions. *J. Chem. Soc. Trans.* **1997**, *93* (5), 885–891. https://doi.org/10.1039/a606453a.

(22) Troe, J. Statistical Adiabatic Channel Model for Ion-Molecule Capture Processes .2. Analytical Treatment of Ion-Dipole Capture. *J. Chem. Phys.* **1996**, *105* (15), 6249–6262. https://doi.org/10.1063/1.472479.

(23) Olzmann, M.; Troe, J. Approximate Determination of Rovibrational Densities of States ρ(E,J) and Numbers of States W(E,J). *Berichte der Bunsengesellschaft für Phys. Chemie* **1994**, *98* (12), 1563–1574. https://doi.org/10.1002/bbpc.19940981210.

(24) Troe, J. Statistical Aspects of Ion-Molecule Reactions. *Adv. Chem. Phys.* **1992**, *82*, 485–529. https://doi.org/10.1002/9780470141403.ch8.

(25) Olzmann, M.; Troe, J. Rapid Approximation of Numbers of Quantum States W(E,J) in the Phase-Space Theory of Unimolecular Bond Fission Reactions. *Berichte Der Bunsen-Gesellschaft-Physical Chem. Chem. Phys.* **1992**, *96* (10), 1327–1332.

(26) Troe, J. Rotational Effects in Complex-Forming Bimolecular Reactions - Application to the Reaction $CH_4 + O_2^+$. *Int. J. Mass Spectrom. Ion Process.* **1987**, *80*, 17–30. https://doi.org/10.1016/0168-1176(87)87019-2.

(27) Troe, J. Statistical Adiabatic Channel Model of Ion Neutral Dipole Capture Rate Constants. *Chem. Phys. Lett.* **1985**, *122* (5), 425–430. https://doi.org/10.1016/0009-2614(85)87240-7.

(28) Ard, S. G.; Melko, J. J.; Ushakov, V. G.; Johnson, R.; Fournier, J. A.; Shuman, N. S.; Guo, H.; Troe, J.; Viggiano, A. A. Activation of Methane by FeO^+: Determining Reaction Pathways through Temperature-Dependent Kinetics and Statistical Modeling. *J. Phys. Chem. A* **2014**, *118* (11), 2029–2039. https://doi.org/10.1021/jp5000705.

(29) Ard, S. G.; Viggiano, A. A.; Shuman, N. S. Old School Techniques with Modern Capabilities:

Kinetics Determination of Dynamical Information Such as Barriers, Multiple Entrance Channel Complexes, Product States, Spin Crossings, and Size Effects in Metallic Ion–Molecule Reactions. *J. Phys. Chem. A* **2021**, *125* (17), 3503–3527. https://doi.org/10.1021/acs.jpca.0c11395.

(30) Sweeny, B. C.; Long, B. A.; Viggiano, A. A.; Ard, S. G.; Shuman, N. S. Effect of Intersystem Crossings on the Kinetics of Thermal Ion-Molecule Reactions: $Ti^+ + O_2$, CO_2, and N_2O. *J. Phys. Chem. A* **2021**, *126*, 859–869.

(31) Baer, T.; Hase, W. L. *Unimolecular Reaction Dynamics: Theory and Experiment*; Oxford: New York, 1996.

(32) Stevens, W.; Sztaray, B.; Shuman, N.; Baer, T.; Troe, J. Specific Rate Constants k(E) of the Dissociation of the Halobenzene Ions: Analysis by Statistical Unimolecular Rate Theories. *J. Phys. Chem. A* **2009**, *113* (3), 573–582. https://doi.org/10.1021/jp807930k.

(33) Troe, J. Rigidity Factors in Unimolecular Reactions. *Berichte Der Bunsen-Gesellschaft-Physical Chem. Chem. Phys.* **1997**, *101* (3), 438–444.

(34) Chesnavich, W. J.; Bowers, M. T. Statistical Phase Space Theory of Polyatomic Systems - Rigorous Energy and Angular-Momentum Conservation in Reactions Involving Symmetric Polyatomic Species. *J. Chem. Phys.* **1977**, *66* (6), 2306–2315. https://doi.org/10.1063/1.434292.

(35) Quack, M.; Troe, J. Specific Rate Constants of Unimolecular Processes 2. Adiabatic Channel Model. *Berichte Der Bunsen-Gesellschaft-Physical Chem. Chem. Phys.* **1974**, *78* (1), 94.

(36) Su, T.; Chesnavich, W. J. Parametrization of the Ion-Polar Molecule Collision Rate Constant by Trajectory Calculations. *J. Chem. Phys.* **1982**, *76* (10), 5183–5185. https://doi.org/10.1063/1.442828.

(37) Owen, C. J.; Keyes, N. R.; Guo, H.; Armentrout, P. B. Bond Dissociation Energy of Au_2^+: A Guided Ion Beam and Theoretical Investigation. *J. Chem. Phys.* **2019**, *150*, 174305.

(38) Sztaray, B.; Bodi, A.; Baer, T. Modeling Unimolecular Reactions in Photoelectron Photoion Coincidence Experiments. *J. Mass Spectrom.* **2010**, *45*, 1233–1245.

(39) Lavrov, V. V; Blagojevic, V.; Koyanagi, G. K.; Orlova, G.; Bohme, D. K. Gas-Phase Oxidation and Nitration of First-, Second-, and Third-Row Atomic Cations in Reactions with Nitrous Oxide: Periodicities in Reactivity. *J. Phys. Chem. A* **2004**, *108*, 5610–5624.

(40) Fisher, E. R.; Elkind, J. L.; Clemmer, D. E.; Georgiadis, R.; Loh, S. K.; Aristov, N.; Sunderlin, L. S.; Armentrout, P. B. Reactions of 4th-Period Metal-Ions (Ca^+ - Zn^+) with O_2: Metal-Oxide Bond Energies. *J. Chem. Phys.* **1990**, *93* (4), 2676–2691. https://doi.org/10.1063/1.458906.

(41) Mlynczak, M. G.; Hunt, L. A.; Mast, J. C.; Marshall, B. T.; Russell III, J. M.; Smith, A. K.; Siskind, D. E.; Yee, J.-H.; Mertens, C. J.; Martin-Torres, F. J.; Thompson, R. E.; Drob, D. P.; Gordley, L. L. Atomic Oxygen in the Mesosphere and Lower Thermosphere Derived from SABER: Algorithm Theoretical Basis and Measurement Uncertainty. *J. Geo. Res. Atmos.* **2013**, *118*, 5724–5735.

(42) Broadley, S.; Vondrak, T.; Wright, T. G.; Plane, J. M. C. A Kinetic Study of Ca-Containing Ions Reacting with O, O_2, CO_2 and H_2O: Implications for Calcium Ion Chemistry in the Upper Atmosphere. *Phys. Chem. Chem. Phys.* **2008**, *10*, 5287–5298.

(43) Bones, D. L.; Gerding, M.; Höffner, J.; Martín, J. C. G.; Plane, J. M. C. A Study of the Dissociative Recombination of CaO^+ with Electrons: Implications for Ca Chemistry in the Upper Atmosphere. *Geophys. Res. Lett.* **2016**, *43* (24), 12333-1,339.

https://doi.org/10.1002/2016GL071755.

(44) Gettelman, A.; Mills, M. J.; Kinnison, D. E.; Garcia, R. R.; Smith, A. K.; Marsh, D. R.; Tilmes, S.; Vitt, F.; Bardeen, C. G.; McInerny, J.; Liu, H.-L.; Solomon, S. C.; Polvani, L. M.; Emmons, L. K.; Lamarque, J.-F.; Richter, J. H.; Glanville, A. S.; Bacmeister, J. T.; Phillips, A. S.; Neale, R. B.; Simpson, I. R.; DuVivier, A. K.; Hodzic, A.; Randel, W. J. The Whole Atmosphere Community Climate Model Version 6 (WACCM6). *J. Geophys. Res.* **2019**, *124*, 12380–12403.

(45) Eyring, V.; Bony, S.; Meehl, G. A.; Senior, C. A.; Stevens, B.; Stouffer, R. J.; Taylor, K. E. Overview of the Coupled Model Intercomparison Project Phase 6 (CMIP6) Experimental Design and Organization. *Geosci. Model Dev.* **2016**, *9*, 1937–1958.

(46) Gerding, M.; Alpers, M.; von Zahn, U.; Rollason, R. J.; Plane, J. M. C. Atmospheric Ca and Ca+ Layers: Midlatitude Observations and Modeling. *J. Geophys. Res.* **2000**, *105*, 27131–27146.

(47) Kopp, E.; Herrmann, U. Ion Composition in the Lower Ionosphere. *Ann. Geophys.* **1984**, *2*, 83–94.

(48) Grebowsky, J. M.; Aikin, A. C. In Situ Measurements of Meteroic Ions. In *Meteors in the Earth's Atmosphere*; Murad, E., Williams, I. P., Eds.; Cambridge University Press: Cambridge, 2002; pp 189–214.